Rheologica Acta
https://doi.org/10.1007/s00397-025-01529-4

ORIGINAL CONTRIBUTION

Leveraging viscoelasticity for load enhancement in rotating contacts

Humayun Ahmed[1] · **Luca Biancofiore**[1,2]

Received: 18 June 2025 / Revised: 29 September 2025 / Accepted: 10 October 2025

Abstract

Tribological components such as bearings and gears sustain a tremendous external load and operate at high relative speeds. For hydrodynamically lubricated contacts, subject to these extreme conditions, the lubricating fluid film exhibits non-Newtonian characteristics. In particular, when the ratio of fluid relaxation time to the flow residence time, i.e., the Deborah number ($\boldsymbol{De}$), becomes appreciable, viscoelastic effects emerge. In this work, we model the effect of viscoelasticity using the viscoelastic Reynolds equation (VR) in cylindrical coordinates under the ultra-dilute limit in which the solvent concentration in terms of viscosity is larger than the polymeric contribution. As such, the velocity field remains Newtonian and the polymer stress constitutive relation is further simplified. We examine the effect of fluid viscoelasticity on the load carrying capacity for two geometries; (i) a conical configuration (that could be aligned or misaligned) and (ii) a flat surface embedded with different kind of textures. Our results show that viscoelasticity can enhance the load carrying capacity in both cases. Small errors in alignment strongly affect the trend in the load versus $\boldsymbol{De}$ and a strong nonlinear trend emerges exhibiting load both saturation and diminishment. Introducing pockets in the surface further improves the load bearing capability beyond the Newtonian values. However, numerical simulation of such textured configurations is challenging and, unlike the inclined asymmetric cone, large values of the Deborah number could not be reached.

Keywords Viscoelasticity · Lubrication theory · Tribology · Thin films

Introduction

Many load-bearing mechanical and biological systems rely on a lubricating mechanism in order to properly function (Tichy and Bou-Saïd 2008). Some examples include contact regions in bearings and gears, human biological joints (spherical hip joint, synovial joint etc), tear film lubrication, all of which comprise two surfaces in relative motion separated by a thin lubricating film. The typical operating conditions, especially in mechanical systems, involve handling a large external load over a small region which causes the film pressure to reach 10^6 Pa in hydrodynamic lubrication and 10^9 Pa in elastohydrodynamic lubrication (Szeri 2010; Sari et al. 2024). Furthermore, the high speed of motion induces large shear stresses in the fluid. These conditions can cause the film to depart from an ideally Newtonian characteristic and exhibit strongly non-Newtonian traits such as shear thinning, viscoelasticity or even viscoplasticity (Mortier et al. 2010; Ahmed and Biancofiore 2022).

From a modeling perspective, the contact regions in these systems span a few millimeters in length (ℓ_x) and a few micrometers in height (H_0), leading to the formation of a thin film (Szeri 2010). The ratio of the characteristic height to length, i.e., the thin-film ratio $\epsilon = \frac{H_0}{\ell_x} << 1$, is small enough to apply the lubrication approximation in the governing set of equations (mass and momentum conservation laws) which gives simplified models for analyzing these systems using computational methods.

Under the conditions where the fluid remains Newtonian, the mathematical models further simplify and yield, in some cases, exact analytical expressions for the film pressure p^*, stress tensor $\boldsymbol{\tau}^*$, and velocity field $\boldsymbol{u}^*$ (see for

---

✉ Luca Biancofiore
luca.biancofiore@univaq.it

Humayun Ahmed
humayun.ahmed@bilkent.edu.tr

[1] Mechanical Engineering Department, Bilkent University, 06800 Ankara, Turkey

[2] Department of Industrial and Information Engineering, and Economics, University of L'Aquila, Piazzale Ernesto Pontieri, Monteluco di Roio, 67100 L'Aquila, Italy

example the one-dimensional plane slider bearing Szeri 2010). For the general case, using numerical techniques, e.g. the finite difference method, the finite element method etc., the solution for the pressure and stress distribution in the film can be obtained. Formulae for practical quantities, relevant for several load bearing applications, such as the load carrying capacity $F_\ell = \int_0^{\ell_x} p^* dx^*$, and surface friction $f_\ell = \int_0^{\ell_x} \tau^*_{xy} dx^*$ immediately follow.

For a rheological perspective, in thin film hydrodynamic lubrication, the high relative sliding velocity of the surfaces U^* leads to a short residence time, ℓ_x/U^*. Industrial grade lubricants and biological fluids, comprising a base Newtonian solvent and polymeric additives that can stretch long distances, then tend to exhibit additional elastic stresses (compared to the purely viscous stresses of the solvent) that require a finite time to relax measured via the polymer relaxation time λ. The fluid film exhibits viscoelastic effects when the Deborah number, i.e., the ratio between the polymer relaxation time and the residence time scale is not negligible $De = \lambda U^*/\ell_x > 0$.

Contrary to the Newtonian formulations for pressure, velocity and stress, the ensuing mathematical models for capturing viscoelasticity are inherently complex. The fundamental governing system of equations now includes a polymer stress constitutive relation (a coupled system of hyperbolic partial differential equations), e.g., the Oldroyd-B model, and replaces the momentum balance by the more general Cauchy's equation of motion. Hence, we have a three-way coupling between the pressure, velocity and stress which is challenging to model computationally and analytically. Nevertheless, for two-dimensional channels, several simplified models have been achieved via clever and meaningful assumptions. For instance, assuming the lubricant is only weakly viscoelastic a classical perturbation in the Deborah number allows linearizing the system of equations (Tichy 1996), and, expansions up to O(De^8) are attainable (Housiadas and Beris 2023) for cases where *De* can reach modest values. Similarly, the reciprocal theorem also allows obtaining meaningful expansions to high *De*-order (Boyko and Stone 2021, 2022) and have been validated against direct numerical simulations. In special cases, through careful consideration of the type of flow and geometry exact analytical solutions for pressure-driven flow (within a reasonable range of the Deborah number) are given for low to moderate values of *De* (Housiadas and Beris 2024). In particular, for solutions in which the polymer viscosity is much smaller than the solvent viscosity, i.e., the ultra-dilute limit, exact analytical expressions for all quantities are attainable for pressure-driven flow via a clever curvilinear coordinate transformation (Boyko et al. 2024). Other notable reduced-order modeling approaches include the generalized Reynolds equations (Johnson and Tevaarwerk 1977), ultra-thin film assumption (Venkatesh et al. 2022), shear stress dominated flow (Akyildiz and Bellout 2004), second-order (or higher) fluid models (Sawyer and Tichy 1998).

For three-dimensional channels, for example, the flow through engineered surfaces, lubricated joints (Tichy and Bou-Saïd 2008) etc., the channel geometry varies along the streamwise and spanwise direction. In these cases, developing simplified models that span a wide range of the Deborah number is especially challenging since the leading-order (Newtonian) solution itself is not analytically accessible.

It is increasingly important to model these contacts because experiments have shown that surface variation can be exploited by placing pocketed textures to further enhance load carrying capacity and minimize surface friction (reducing shear stress and mitigating the effects of shear thinning) (Schuh and Ewoldt 2016; Hoon Lee et al. 2017; Schuh et al. 2017; Schuh and Ewoldt 2019; Lee et al. 2019). In particular, a simplified mathematical framework using the Criminale-Ericksen-Filbey (CEF) model (Bird et al. 1987) showed potential in modeling textured surfaces in cylindrical coordinates using the pseudo-spectral method (Schuh et al. 2017) and paved the way for optimizing the texture design, maximizing load and minimizing frictional losses (Hoon Lee et al. 2017). Although, the CEF equation is suitable for problems involving variable properties (for instance, shear thinning), it builds upon the order-fluid model for capturing the viscoelasticity of the fluid (Owens and Phillips 2002).

An alternative is the recent viscoelastic Reynolds numerical method which constitutes a single partial differential equation for the pressure in terms of the fluid extra stress components (Ahmed and Biancofiore 2025). A key feature is the decoupling of the pressure, velocity and stress components which greatly simplifies the computational cost. The decoupling is achieved by an a priori estimate of the velocity field by assuming a weak linear perturbation to the flow which has been numerically verified via direct numerical simulations (DNS) (Ahmed and Biancofiore 2021, 2023, 2025) and experimental evidence albeit for different flow configurations is also available (Phan-Thien and Tanner 1983; Zhang et al. 2023; Zheng et al. 2023). In fact, experiments on thin films formed by bubbles laden with surfactant show no influence of viscoelasticity on the drainage dynamics (Lombardi et al. 2025b, a). The ultra-dilute approximation well-known in modeling non-Newtonian fluid flow (Moore and Shelley 2012) has been recently applied to pressure driven thin-film flow (Boyko et al. 2024) and offers another promising alternative that can achieve a full decoupling of the velocity field from the pressure and fluid extra stress.

In this work, we utilize the viscoelastic Reynolds numerical approach (VR) for modeling the viscoelastic flow through channel geometries conforming ideally to cylindrical coordinates using the Oldroyd-B and Giesekus constitutive relations in the ultra-dilute limit. We examine an untextured inclined surface, mimicking a (mis)aligned rheometer, and two types of textured pads: (i) one with straight cylindrical pockets and (ii) one with inclined pockets, following Schuh and Ewoldt (2016). We compare and contrast the variation in the load carrying capacity as the strength of viscoelasticity is varied (via the Deborah number), and also examine the influence of secondary nonlinear effects such as finite polymer extension and shear thinning which are absent from the classical Oldroyd-B constitutive relation.

The paper is organized as follows. Section "Mathematical and numerical formulation" deals with the mathematical model included some information about the numerical details. The results for the pressure, load and friction are presented in Section "Results and discussion". In particular, the inclined (mis)aligned conical configuration, and the textured pad are discussed in Sections "Cone-and-plate geometry" and "Textured pad", respectively. Finally, conclusions are drawn in Section "Conclusions and future work" with recommendations for potential future work.

Mathematical and numerical formulation

In this section, we present the governing system of equations that mathematically describe the flow of a viscoelastic fluid through a thin channel. Using lubrication theory, and the ultra-dilute assumption (Boyko et al. 2024), we arrive to a single differential equation, the viscoelastic Reynolds numerical approach (VR), see Section "Viscoelastic Reynolds model", for determining the pressure in cylindrical coordinates. It is adapted and modified from previous works in a Cartesian domain (Ahmed and Biancofiore 2021, 2023, 2025), which allows predicting the pressure distribution for two- and three-dimensional configurations.

Governing equations

The governing system of equations for the flow of a viscoelastic fluid in a thin channel consists of the mass conservation equation and Cauchy's equation of motion,

$$\boldsymbol{\nabla}^* \cdot \mathrm{u}^* = 0, \tag{1a}$$

$$\rho \frac{D(\mathrm{u}^*)}{Dt^*} = -\boldsymbol{\nabla}^* p^* + \boldsymbol{\nabla}^* \cdot \boldsymbol{\sigma}^*, \tag{1b}$$

$$\boldsymbol{\tau}^* + \lambda \overset{\triangledown}{\boldsymbol{\tau}}{}^* = 2\eta_p \mathrm{D}^*, \tag{1c}$$

$$\boldsymbol{\sigma}^* = 2\eta_s \mathrm{D}^* + \boldsymbol{\tau}^*, \tag{1d}$$

where, $\boldsymbol{u}^*$ is the velocity field, p^* is the pressure, $\boldsymbol{\sigma}^*$ is the total stress tensor, $\boldsymbol{\tau}^*$ is the polymer extra stress tensor, η_s is the solvent viscosity, η_p is the polymer viscosity, $\boldsymbol{D}^* = 1/2(\boldsymbol{\nabla}^* \boldsymbol{u}^* + \boldsymbol{\nabla}^* \boldsymbol{u}^{*T})$ is the deformation rate tensor, $\overset{\triangledown}{\boldsymbol{\tau}}{}^* = \frac{D\boldsymbol{\tau}^*}{Dt^*} - \boldsymbol{L}^*\boldsymbol{\tau}^* - \boldsymbol{\tau}^*\boldsymbol{L}^{*T}$ is the upper convected rate operator, $\boldsymbol{L}^* = \boldsymbol{\nabla}^* \boldsymbol{u}^*$ is the velocity gradient tensor.

Equation 1c represents the Oldroyd-B constitutive relation that captures the viscoelastic contribution of the fluid. However, it excludes any secondary effects such as shear thinning and finite extension of the polymers (Bird et al. 1987). To account for these two affects, the Giesekus model

$$\boldsymbol{\tau}^* + \lambda \overset{\triangledown}{\boldsymbol{\tau}}{}^* + \alpha \frac{\lambda}{\eta_p} \boldsymbol{\tau}^* \boldsymbol{\tau}^* = 2\eta_p \mathrm{D}^*, \tag{2}$$

where, $0 < \alpha < 1$ is the mobility parameter, is also employed in this study. Equation 2 is also used for validating the results against published work (Hoon Lee et al. 2017). The robust approach is the direct numerical simulation of the full set of equations. However, this poses significant challenges due to the high Weissenberg number problem (HWNP) (Fattal and Kupferman 2004) and is computationally expensive owing to the numerical constraints of a thin film, strongly reducing the mesh spacing and the time step size.

Thin film equations

A set of thin-film reduced equations are derived for a lubricated channel of radius R_0 and height $h^*(r^*, \theta)$ modeled via the cylindrical coordinate system (r^*, θ, z^*). Using the scaling

$$r^* = R_0 r, \qquad z^* = H_0 z, \qquad h^* = H_0 h, \qquad \epsilon = \frac{H_0}{R_0}, \tag{3a}$$

$$u_r^* = U_0 u_r, \qquad u_\theta^* = U_0 u_\theta, \qquad u_z^* = \epsilon U_0 u_z, \tag{3b}$$

$$\tau_{rr}^* = \tau_{rr} \frac{\eta_0 U_0 R_0}{H_0^2}, \qquad \tau_{\theta r}^* = \tau_{\theta r} \frac{\eta_0 U_0}{H_0}, \qquad \tau_{zr}^* = \tau_{zr} \frac{\eta_0 U_0}{H_0}, \tag{3c}$$

$$\tau_{\theta\theta}^* = \tau_{\theta\theta} \frac{\eta_0 U_0 R_0}{H_0^2}, \qquad \tau_{z\theta}^* = \tau_{z\theta} \frac{\eta_0 U_0}{H_0}, \qquad \tau_{zz}^* = \tau_{zz} \frac{\eta_0 U_0}{R_0}, \tag{3d}$$

$$\begin{gathered} p^* = \frac{\eta_0 U_0 R_0}{H_0^2} p, \qquad De = \lambda \frac{U_0}{R_0}, \\ \beta = \frac{\eta_s}{\eta_0}, \qquad \eta_0 = \eta_s + \eta_p \end{gathered} \tag{3e}$$

where, H_0 is the film height, R_0 is the characteristic length (radius), U_0 is the reference velocity (equivalently $U_0 = R_0 \Omega_0$ for some rotation rate Ω_0). The scalar components for the tensor equations are given in Ref. Owens and Phillips (2002).

Substituting Eqs. 3a-3e into the governing system of Eqs. 1a-1d and applying the lubrication limit $\epsilon^2 \to 0$, gives the reduced set of dimensionless scalar equations,

$$\frac{1}{r}\frac{\partial (r u_r)}{\partial r} + \frac{1}{r}\frac{\partial u_\theta}{\partial \theta} + \frac{\partial u_z}{\partial z} = 0, \tag{4a}$$

$$\frac{\partial p}{\partial r} = \beta \frac{\partial^2 u_r}{\partial z^2} + \frac{1}{r}\frac{\partial}{\partial r}(r\tau_{rr}) + \frac{1}{r}\frac{\partial \tau_{\theta r}}{\partial \theta} + \frac{\partial \tau_{zr}}{\partial z} - \frac{\tau_{\theta\theta}}{r}, \tag{4b}$$

$$\frac{1}{r}\frac{\partial p}{\partial \theta} = \beta \frac{\partial^2 u_\theta}{\partial z^2} + \frac{1}{r^2}\frac{\partial}{\partial r}(r^2\tau_{r\theta}) + \frac{1}{r}\frac{\partial \tau_{\theta\theta}}{\partial \theta} + \frac{\partial \tau_{z\theta}}{\partial z}, \tag{4c}$$

$$\frac{\partial p}{\partial z} = 0, \tag{4d}$$

$$\tau_{rr} + De\left(\frac{\partial \tau_{rr}}{\partial t} + u_r\frac{\partial \tau_{rr}}{\partial r} + \frac{u_\theta}{r}\frac{\partial \tau_{rr}}{\partial \theta} + u_z\frac{\partial \tau_{rr}}{\partial z} - 2\frac{u_\theta}{r}\tau_{\theta r}\right) \tag{4e}$$

$$\begin{gathered} - De\left(2\tau_{rr}\frac{\partial u_r}{\partial r} + \frac{2}{r}\tau_{\theta r}\frac{\partial u_r}{\partial \theta} + 2\tau_{zr}\frac{\partial u_r}{\partial z} - \frac{2}{r}u_\theta\right) = 0, \\ \tau_{\theta r} + De\left(\frac{\partial \tau_{\theta r}}{\partial t} + u_r\frac{\partial \tau_{\theta r}}{\partial r} + \frac{u_\theta}{r}\frac{\partial \tau_{\theta r}}{\partial \theta} + u_z\frac{\partial \tau_{\theta r}}{\partial z} - \frac{u_\theta}{r}(\tau_{\theta r} - \tau_{\theta\theta})\right) \end{gathered} \tag{4f}$$

$$\begin{gathered} - De\left(\tau_{rr}\frac{\partial u_\theta}{\partial r} + \tau_{zr}\frac{\partial u_\theta}{\partial z} + \tau_{\theta r}\frac{\partial u_r}{\partial r} + \tau_{z\theta}\frac{\partial u_r}{\partial z} + \frac{u_r\tau_{\theta r}}{r} - \frac{u_\theta\tau_{\theta\theta}}{r} \right. \\ \left. + \frac{\tau_{\theta r}}{r}\frac{\partial u_\theta}{\partial \theta} + \frac{\tau_{\theta\theta}}{r}\frac{\partial u_r}{\partial \theta}\right) = 0, \\ \tau_{zr} + De\left(\frac{\partial \tau_{zr}}{\partial t} + u_r\frac{\partial \tau_{zr}}{\partial r} + \frac{u_\theta}{r}\frac{\partial \tau_{zr}}{\partial \theta} + u_z\frac{\partial \tau_{zr}}{\partial z} - \frac{u_\theta}{r}\tau_{\theta z}\right) \end{gathered} \tag{4g}$$

$$\begin{gathered} - De\left(\tau_{rr}\frac{\partial u_z}{\partial r} + \tau_{zr}\frac{\partial u_r}{\partial r} + \tau_{zr}\frac{\partial u_z}{\partial z} + \tau_{zz}\frac{\partial u_r}{\partial z} - \frac{u_\theta\tau_{\theta z}}{r} + \frac{\tau_{\theta r}}{r}\frac{\partial u_z}{\partial \theta} \right. \\ \left. + \frac{\tau_{\theta z}}{r}\frac{\partial u_r}{\partial \theta}\right) = (1-\beta)\frac{\partial u_r}{\partial z}, \\ \tau_{\theta\theta} + De\left(\frac{\partial \tau_{\theta\theta}}{\partial t} + u_r\frac{\partial \tau_{\theta\theta}}{\partial r} + \frac{u_\theta}{r}\frac{\partial \tau_{\theta\theta}}{\partial \theta} + u_z\frac{\partial \tau_{\theta\theta}}{\partial z} + 2\frac{u_\theta}{r}\tau_{\theta r}\right) \end{gathered} \tag{4h}$$

$$\begin{gathered} - De\left(2\tau_{\theta r}\frac{\partial u_\theta}{\partial r} + 2\tau_{\theta z}\frac{\partial u_\theta}{\partial z} + 2\frac{u_r\tau_{\theta\theta}}{r} + 2\frac{\tau_{\theta\theta}}{r}\frac{\partial u_\theta}{\partial \theta}\right) = 0, \\ \tau_{z\theta} + De\left(\frac{\partial \tau_{z\theta}}{\partial t} + u_r\frac{\partial \tau_{z\theta}}{\partial r} + \frac{u_\theta}{r}\frac{\partial \tau_{z\theta}}{\partial \theta} + u_z\frac{\partial \tau_{z\theta}}{\partial z} + \frac{u_\theta}{r}\tau_{zr}\right) \end{gathered} \tag{4i}$$

$$\begin{gathered} - De\left(\tau_{zr}\frac{\partial u_\theta}{\partial r} + \tau_{r\theta}\frac{\partial u_z}{\partial r} + \tau_{zz}\frac{\partial u_\theta}{\partial z} + \tau_{\theta z}\frac{\partial u_z}{\partial z} + \frac{u_r\tau_{\theta z}}{r} + \frac{\tau_{\theta z}}{r}\frac{\partial u_\theta}{\partial \theta} \right. \\ \left. + \frac{\tau_{\theta\theta}}{r}\frac{\partial u_z}{\partial \theta}\right) = (1-\beta)\frac{\partial u_\theta}{\partial z}, \\ \tau_{zz} + De\left(\frac{\partial \tau_{zz}}{\partial t} + u_r\frac{\partial \tau_{zz}}{\partial r} + \frac{u_\theta}{r}\frac{\partial \tau_{zz}}{\partial \theta} + u_z\frac{\partial \tau_{zz}}{\partial z}\right) \\ - De\left(2\tau_{rz}\frac{\partial u_z}{\partial r} + 2\tau_{zz}\frac{\partial u_z}{\partial z} + 2\frac{\tau_{\theta z}}{r}\frac{\partial u_z}{\partial \theta}\right) = 0, \end{gathered} \tag{4j}$$

where, $\eta_0 = \eta_s + \eta_p$ is the total viscosity of the fluid. Equations 4a-4j comprise a coupled system of nonlinear partial differential equations. The classical lubrication result of constant pressure across the film is clearly retrieved, but the numerical solution is still challenging because of the three-way coupling of p, $\boldsymbol{u}$ and $\boldsymbol{\tau}$.

Note that the Newtonian system of equations ($p = p^{(0)}$, $\boldsymbol{u} = \boldsymbol{u}^{(0)}$ and $\boldsymbol{\tau} = \boldsymbol{\tau}^{(0)}$) is obtained by setting $De = 0$ in Eqs. 4a-4j (and simplifying),

$$\frac{1}{r}\frac{\partial (r u_r^{(0)})}{\partial r} + \frac{1}{r}\frac{\partial u_\theta^{(0)}}{\partial \theta} + \frac{\partial u_z^{(0)}}{\partial z} = 0, \tag{5a}$$

$$\frac{\partial p^{(0)}}{\partial r} = \frac{\partial^2 u_r^{(0)}}{\partial z^2}, \tag{5b}$$

$$\frac{1}{r}\frac{\partial p^{(0)}}{\partial \theta} = \frac{\partial^2 u_\theta^{(0)}}{\partial z^2}, \tag{5c}$$

$$\frac{\partial p^{(0)}}{\partial z} = 0. \tag{5d}$$

This simplified system is solved subject to the boundary conditions for a sliding (rotating about the *z*-axis) lubricated channel,

$$u_r^{(0)}(r, \theta, z = 0) = 0, \quad u_r^{(0)}(r, \theta, z = h) = 0, \tag{6a}$$

$$u_\theta^{(0)}(r, \theta, z = 0) = r, \quad u_\theta^{(0)}(r, \theta, z = h) = 0, \tag{6b}$$

$$u_z^{(0)}(r, \theta, z = 0) = 0, \quad u_z^{(0)}(r, \theta, z = h) = 0, \tag{6c}$$

to give explicit equations for the Newtonian pressure and velocity components,

$$\frac{1}{r}\frac{\partial}{\partial r}\left(\frac{r h^3}{12}\frac{\partial p^{(0)}}{\partial r}\right) + \frac{1}{r}\frac{\partial}{\partial \theta}\left(\frac{h^3}{12 r}\frac{\partial p^{(0)}}{\partial \theta}\right) = \frac{1}{2}\frac{\partial h}{\partial \theta}, \tag{7a}$$

$$u_r^{(0)} = \frac{1}{2}\frac{\partial p^{(0)}}{\partial r}(z^2 - zh), \tag{7b}$$

$$u_\theta^{(0)} = \frac{1}{2r}\frac{\partial p^{(0)}}{\partial \theta}(z^2 - zh) + r\left(1 - \frac{z}{h}\right), \tag{7c}$$

$$\begin{aligned} u_z^{(0)} = {} & z^3\left(-\frac{1}{6}\frac{\partial^2 p}{\partial r^2} - \frac{1}{6r}\frac{\partial p^{(0)}}{\partial r} - \frac{1}{6r^2}\frac{\partial^2 p}{\partial \theta^2}\right) \\ & + z^2\left(\frac{h}{4}\frac{\partial^2 p^{(0)}}{\partial r^2} + \frac{1}{4}\frac{\partial h}{\partial r}\frac{\partial p^{(0)}}{\partial r} + \frac{1}{2h^2}\frac{\partial p^{(0)}}{\partial \theta} \right. \\ & \left. + \frac{h}{4r}\frac{\partial p^{(0)}}{\partial r} + \frac{h}{4r^2}\frac{\partial^2 p^{(0)}}{\partial \theta^2} + \frac{1}{4r^2}\frac{\partial h}{\partial \theta}\frac{\partial p^{(0)}}{\partial \theta}\right). \end{aligned} \tag{7d}$$

The pressure distribution from Eq. 7a is obtained using any of the classical numerical methods, for example, the finite difference method, subject to the boundary conditions for a periodic domain

$$\frac{\partial p^{(0)}}{\partial r}(r=0,\theta)=0, p^{(0)}(r=1,\theta)=0, \\ and\ p^{(0)}(r,\theta=0)=p^{(0)}(r,\theta=2\pi). \tag{8}$$

To obtain the pressure distribution in the viscoelastic case, one can solve the reduced system of Eqs. 4a-4j which is challenging for the three-dimensional case and for complex geometries. An alternative method is the viscoelastic Reynolds numerical approach in which an integral-differential form of the pressure equation is obtained (Ahmed and Biancofiore 2021), see Section "Viscoelastic Reynolds model" for details.

Viscoelastic Reynolds model

In this section, we present a reduced-order approach that comprises (i) a one-way coupled approach mitigating the costly iterative approach for the fully coupled system of equations (Eqs. 4a-4j) and (ii) the viscoelastic Reynolds equation (VR), a single integral differential equation for the pressure that replaces the continuity, r-momentum and θ -momentum equations altogether.

The pressure equation has the form

$$\frac{1}{r}\frac{\partial}{\partial r}\left(\frac{rh^3}{12}\frac{\partial p}{\partial r}\right)+\frac{1}{r}\frac{\partial}{\partial \theta}(\frac{h^3}{12}\frac{\partial p}{\partial \theta})=\frac{1}{r}\frac{\partial \mathcal{G}}{\partial \theta}+\frac{1}{r}\frac{\partial (r\mathcal{F})}{\partial r}, \tag{9a}$$

$$\begin{aligned}\mathcal{F}=\frac{h^3}{2}&\overline{\left[(Z-Z^2)\frac{1}{r}\frac{\partial (r\tau_{rr})}{\partial r}\right]}\\ &+\frac{h^2}{2}\overline{[(2Z-1)\tau_{rz}]}+\\ &\frac{h^3}{2}\overline{\left[(Z-Z^2)\frac{1}{r}\frac{\partial \tau_{r\theta}}{\partial \theta}\right]}\end{aligned} \tag{9b}$$

$$-\frac{h^3}{2}\overline{\left[(Z-Z^2)\frac{\tau_{\theta\theta}}{r}\right]},$$

$$\begin{aligned}\mathcal{G}=\frac{\beta}{2}rh+\frac{h^3}{2}\overline{\left[(Z-Z^2)\frac{1}{r^2}\frac{\partial (r^2\tau_{r\theta})}{\partial r}\right]}+\frac{h^2}{2}\overline{[(2Z-1)\tau_{z\theta}]}\\ +\frac{h^3}{2}\overline{\left[(Z-Z^2)\frac{1}{r}\frac{\partial \tau_{\theta\theta}}{\partial \theta}\right]}.\end{aligned} \tag{9c}$$

where, $Z=z/h$. The details regarding the derivation are presented in Appendix A and are no different from the Cartesian case presented in Ahmed and Biancofiore (2021). Note (i) the resemblance to the Newtonian form of Eq. 7a and the generalized Reynolds equation (Dowson and Taylor 1979; Ahmed and Biancofiore 2022) and (ii) the explicit dependence of pressure gradients on the components of the viscoelastic stress. Next, we demonstrate how to decouple the pressure from the stress components.

There are several ways to achieve one-way coupling. For example, in sliding two-dimensional configurations (Li 2014) or pressure-driven flows (Boyko and Stone 2022), having equal inlet and outlet channel heights causes the velocity field of *De*-order (and higher) to vanish point-wise in the channel. Furthermore, for weakly viscoelastic cases, the velocity field deviates weakly from the Newtonian limit (Tanner 1969; Phan-Thien and Tanner 1983) which is especially observable for squeeze film lubrication (Zhang et al. 2023; Zheng et al. 2023).

In this work, in order to decouple Eqs. 4a-4j and remain in the high *De*-limit, we apply the ultra-dilute assumption (Boyko et al. 2024) in which the concentration of solvent is large, i.e., $(1-\beta)<<1$ and, as a result, the $(1-\beta)$-order velocity field is Newtonian, but the Deborah number can acquire any value. This allows a unique decoupling of the fluid stress equations from the velocity field, and, also the pressure as well, but in the limit of high solvent concentration ratio β. It should be stated that in the original work, analytical solutions for the stress components at the $(1-\beta)$-order are obtained through a clever transformation of the coordinate system for a two-dimensional pressure driven flow.

To solve for the film pressure, the fluid stress distribution (an unknown in Eq. 9a) is obtained via the constitutive relation using the following boundary conditions

$$\frac{\partial \tau_{ij}}{\partial r}(r=0,\theta,z)=0, \tag{10a}$$

$$\tau_{ij}(r,\theta=0,z)=\tau_{ij}(r,\theta=2\pi,z), \tag{10b}$$

$$\tau_{ij}(r,\theta,h)+De\left(\left(\frac{\partial \tau_{ij}(r,\theta,h)}{\partial t}-L_{ik}(r,\theta,h)\tau_{kj}(r,\theta,h)-\tau_{ik}(r,\theta,h)L_{jk}(r,\theta,h)\right)=\hat{D}_{ij}(r,\theta,h). \tag{10c}$$

where, L_{ij} is the velocity gradient, D_{ij} is the thin-film reduced deformation gradient tensor (Eqs. 4e-4j), and initial condition $\tau_{ij}(r,\theta,z)=2(1-\beta)\hat{D}_{ij}$ which assumes the stress is initially Newtonian. Equation 10c is obtained by setting

$$u_r^{(0)}(r,\theta,h)=0, \qquad u_\theta^{(0)}(r,\theta,h)=0, \qquad u_z^{(0)}(r,\theta,h)=0, \tag{11}$$

in the scalar stress component relations.

The full viscoelastic problem reduces to (i) estimating the fluid velocity (Eqs. 7b-7d), (ii) solving the constitutive relation for the fluid extra stress (Eqs. 4e-4j), subject to the boundary conditions Eqs. 10a-10c and, finally, (iii) predicting the pressure using the VR model (Eqs. 9a). The pressure is then integrated over the domain to obtain the load carrying capacity

$$F_\ell = \int_0^1 \int_0^{2\pi} pr \, dr d\theta, \tag{12}$$

and the friction on the lower flat plate

$$f_\ell = \int_0^1 \int_0^{2\pi} \left(\beta \frac{\partial u_\theta^{(0)}}{\partial z} + \tau_{\theta z} \right) r \, dr d\theta. \tag{13}$$

Numerical method

In this work, we pursue the classical finite difference method (FDM) for the numerical solution of the equations presented in Section "Viscoelastic Reynolds model" owing to its simplicity and amenability to implicit treatment. A transformation of the physical domain, $\boldsymbol{r} = (r, \theta, z)$, to a computational domain, $\boldsymbol{R} = (R, \Theta, Z)$,

$$r = R, \qquad \theta = \Theta, \qquad z = Zh(r, \theta), \tag{14}$$

is required for direct application of the FDM. Using the relation

$$\frac{\partial q}{\partial R_k} = \frac{\partial q}{\partial r_s} \frac{\partial r_s}{\partial R_k}, \tag{15}$$

where, $q = \{p, u_i, \tau_{ij}\}$, the derivative operators in the constitutive relations are transformed into the computational domain for which we can freely choose a uniform mesh or unit box. The finite difference stencils for the derivatives can be easily found in literature (Hirsch 2007) and are not presented here.

The textured pad described in Section "Textured pad" requires careful implementation of derivatives in θ. Using a central difference scheme gives erroneous results. Therefore for the textured pad, a simple first-order forward or backward scheme (depending on the texture orientation) is employed, and since the inclination of the textures is strictly linear, the first-order derivative of the surface becomes exact. For the conical geometry (see Section "Cone-and-plate geometry"), this issue can be ignored and we employ fourth-order accurate schemes throughout.

The constitutive relations are transient but the problems considered here have a steady state and upon satisfying the condition $||\tau_{ij}^{(k+1)} - \tau_{ij}^{(k)}|| < 10^{-12}$ the algorithm terminates, where, k is the iteration (or time) level. For the smooth conical surface (see Section "Cone-and-plate geometry"), $(N_r, N_\theta, N_z) = (96, 32, 96)$ is sufficient for grid independent solutions, and $(N_r, N_\theta, N_z) = (384, 32, 384)$ is required for the textured surface (see Section "Textured pad").

Results and discussion

In this section, we present the results for the load carrying capacity and friction for two different surface configurations; (i) an inclined (untextured) surface mimicking a cone-and-plate rheometer adapted from Ref. Lee et al. (2019) (see Section "Cone-and-plate geometry") and (ii) a circular plate embedded with cylindrical textures straight or inclined at angles β_t (see Section "Textured pad"). For each of these cases, we investigate the influence of geometric parameters, the angle of inclination of the cone, influence (mis)alignment and the texture angle on the load carrying capacity and friction on the lower plate.

Cone-and-plate geometry

In this section, we investigate the dependency of the load and friction on the viscoelasticity of the fluid. We focus on a smooth inclined conical surface that mimics a cone-and-plate rheometer. Although surfaces in practice may be considered sufficiently smooth and assumed to be symmetric about the vertical axis, it is possible to incur a small degree of misalignment leading to gradients along the circumferential direction. If the misalignment is small enough, it can be safely ignored for the Newtonian fluid. However, viscoelastic fluids respond strongly to surface gradients and can lead to vastly different predictions.

Geometry

The cone-and-plate configuration is modeled using

$$h = 1 + r \tan(\delta)(1 + e \cos(\theta)), \tag{16}$$

where, δ is the angle of inclination (in degrees) and e is a coefficient ($e \geq 0$) that controls the degree of misalignment. Figure 1 shows the geometry for an inclined cone ($\delta = 20°$): (a) perfectly aligned $e = 0$ and (b) with misalignment $e = 0.75$. Both configurations are reported in Fig. 1c for $\theta = 0$ and $\theta = \pi$. For a better depiction of the figures involving the cylindrical coordinates, we report them using the Cartesian coordinates: $x = r \sin(\theta)$ and $y = r \cos \theta$. If

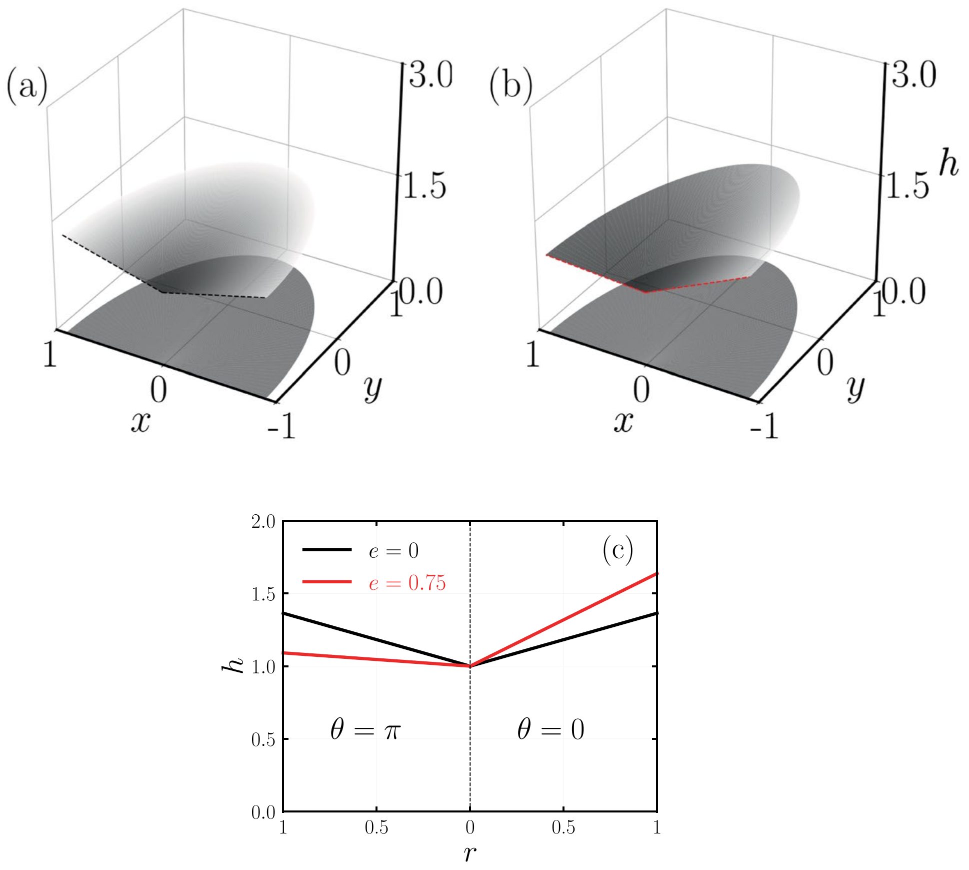

Fig. 1 A conical geometry mimicking a cone-and-plate rheometer for (a) a fully aligned case with $e = 0$ and (b) a misaligned case with $e = 0.75$ using $\delta = 20^\circ$. (c) The two configurations for $\theta = 0, \pi$

Table 1 The dimensional parameters used for validation of the VR model against experimental data for the torque taken from Lee et al. (2019)

Parameter	Value
Outer radius (R_0)	20 mm
Rotation rate (Ω_0)	10 rad/s
Gap (h_0)	269 μm
Solvent viscosity (η_s)	9.624 mPa.s
Solvent density (ρ_s)	873.4 kg/m^3

$e > 0$, we have surface gradients (smoothly varying) along both the radial and circumferential direction.

Aligned configuration cone ($e = 0$)

A slightly inclined flat conical surface can be used to represent a fully aligned cone-and-plate rheometer. Aside from its practical significance in modeling a cone-and-plate type rheometer, Eq. 16 carries also several computational advantages. The shear rate in the channel is purely Couette

$$\dot{\gamma}_{\theta z} = \frac{\partial u_\theta}{\partial z} = -\frac{1}{h(r)}, \tag{17}$$

and the invariance of the h along θ allows enforcing $\frac{\partial}{\partial \theta} = 0$. An immediate consequence is the zero net load generation in the Newtonian case (the right hand side vanishes completely in Eq. 7a) and in the viscoelastic case, the linear stress constitutive relations such as the Oldroyd-B reduce to

$$\begin{aligned} &\tau_{rr} = 0, && \tau_{r\theta} = 0, && \tau_{rz} = 0, \\ &\tau_{\theta\theta} = 2De(1-\beta)\dot{\gamma}_{\theta z}^2, && \tau_{\theta z} = (1-\beta)\dot{\gamma}_{\theta z}, && \tau_{zz} = 0. \end{aligned} \tag{18}$$

These relations can be used to validate the results for the Oldroyd-B model and the numerical method. For nonlinear models, a numerical approach should be adopted. The purpose here is to assess the efficacy of the VR approach coupled with the ultra-dilute assumption which, in theory, allows reaching large values of the Deborah number (for large β).

Before proceeding, we validate our model against the results presented by Lee et al. (2019) for the dimensional friction (which they call torque) on the lower plate

$f_\ell^* = \int_0^{R_0} \int_0^{2\pi} r^{*2} \tau_{\theta z^*}^* |_{z^*=0} dr^* d\theta$. The dimensional parameters used for the comparison are taken from the supplementary material of the original study (Lee et al. 2019) and are shown in Table 1. The variation in the net torque versus the rotation rate of the cone (Ω) is shown in Fig. 2 for the Oldroyd-B and the Giesekus models using the VR model. We find a good agreement for the net torque produced (after

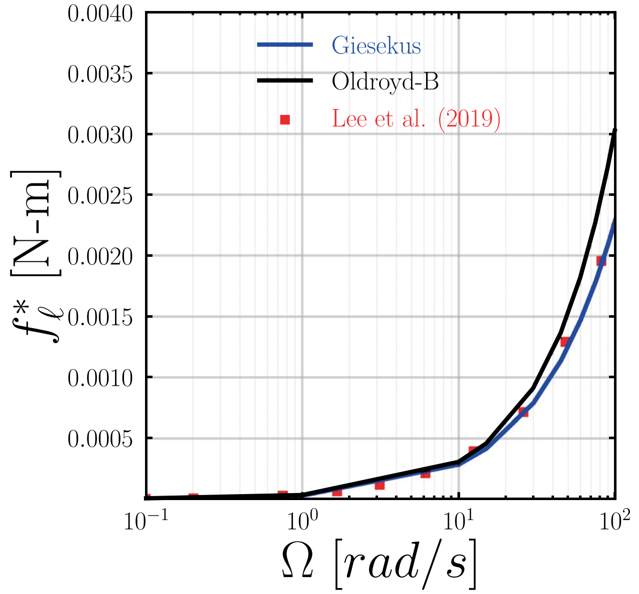

Fig. 2 The dimensional friction f_ℓ^* predicted versus the angular rate of rotation for the Oldroyd-B and Giesekus model using the VR model compared against the results presented in the supplementary material from Lee et al. (2019)

considering the dimensional parameters contained in the original work) versus the rotation speed.

Figure 3 shows the variation in the scaled net vertical force versus the angle of inclination of the cone for different values of *De*, $\alpha = 0.01$, and $\beta = 0.8$. As expected, the Oldroyd-B model predicts a linear scaling of the net vertical force and the net torque. However, the Giesekus model accounts for shear thinning and finite polymer extension through an additional parameter α, and, as we modify the net shear rate through the cone angle, the results no longer collapse onto a single curve. The strength of the shear thinning effect, proportional to the Deborah number, reduces the lift and torque as expected. Oddly, for a diverging cone ($\delta > 0°$), the shear rate in the channel, reduces but the predicted load and torque are lower compared to a convergent cone for the same angle.

The load increase shown in Fig. 3 is due to the generation of circumferential stress $\tau_{\theta\theta}$ which varies radially. In Eqs. 9a, setting $\frac{\partial}{\partial\theta} = 0$ and using Eqs. 18, the pressure distribution becomes a function of the circumferential (normal) stress

$$r\frac{\partial p}{\partial r} = \frac{1}{2}\tau_{\theta\theta} + K, \tag{19}$$

where, K is a constant of integration. The precise analytical expression is not of interest, but can be achieved by continuing the integration. More importantly, the explicit dependence of the pressure gradient on the normal stress is apparent. As normal stresses increase, pressure immediately follows.

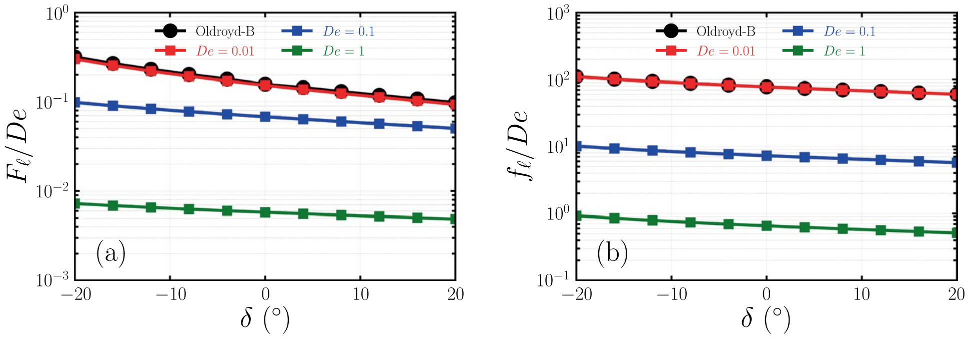

Fig. 3 The variation in the (a) net vertical force and (b) the friction on the pad scaled with *De* versus the cone inclination angle for the Oldroyd-B (black line) and the Giesekus (with $\alpha = 0.01$) constitutive relations for three different values of the Deborah number $\beta = 0.8$. Note that Oldroyd-B is a linear model in the stress and all the curves then collapse onto the black line

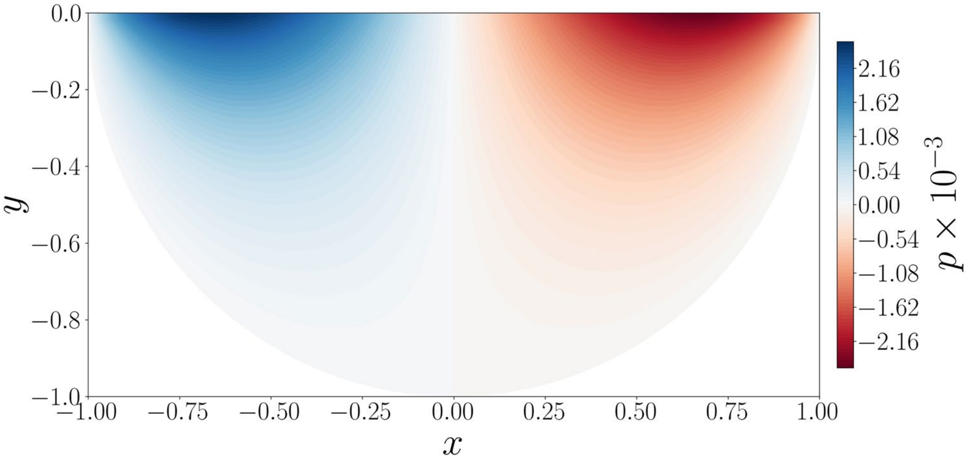

Fig. 4 The Newtonian pressure distribution across a misaligned conical configuration for $\delta = 1.011°$ and $e = 0.5$

Fig. 5 The variation in the load (solid lines) and friction (dashed lines) versus (a) the Deborah number for $e = 0.5$ and (b) the misalignment factor *e* for $De = 0.1$ for the Giesekus model for different values of α using $\beta = 0.8$ and $\delta = 1.011°$

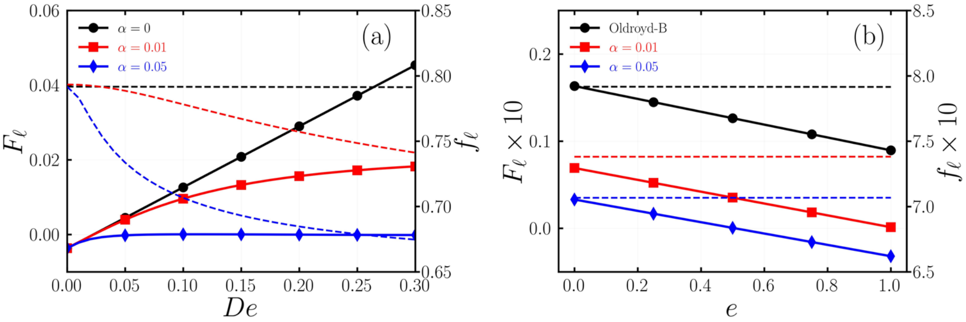

Fig. 6 The pressure distribution across the tilted misaligned conical pad for (a) $De = 0$, (b) $De = 0.25$, (c) $De = 0.5$, (d) $De = 0.75$, (e) $De = 1$, (f) $De = 1.25$ for $\delta = 1.011°$, $e = 1$, $\beta = 0.8$, and $\alpha = 0$

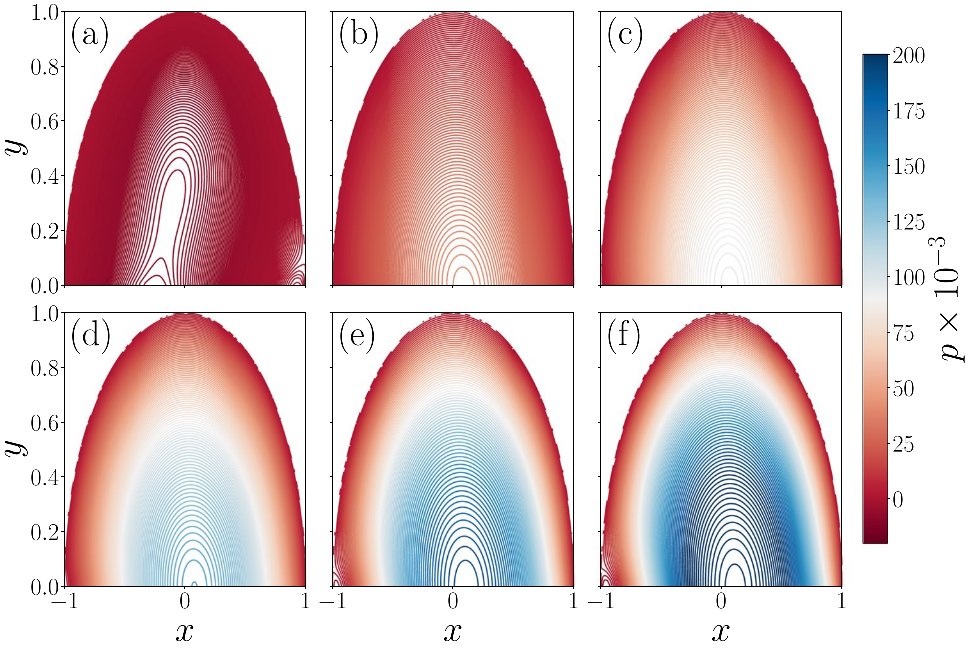

Misaligned cone-and-plate rheometer ($e > 0$)

We introduce a tilt in the surface that allows circumferential variation of the surface height and, consequently, all dependent quantities. Practically, this would represent a misaligned cone-and-plate rheometer, see Fig. 1b. For very small values of *e* (Eq. 16) the plates are slightly tilted but the Newtonian pressure distribution across the channel, shown in Fig. 4, is now finite. Although the pressure reaches finite values (equal parts positive and negative), the load for the small tilt is zero indicating that $e \sim O(1)$ is insufficient to induce any asymmetry in the pressure.

Next, we examine the viscoelastic case using the Giesekus (single mode) constitutive relation but for a very small misalignment. Figure 5 compares the load carrying capacity and the friction for a slightly tilted and nearly flat ($\delta = 1.011°$) cone versus the Deborah number (Fig. 5a) with fixed tilt $e = 0.5$, and versus the tilt factor with $De = 0.1$ (Fig. 5b). Note that the $\alpha = 0$ case, i.e. the black lines in Fig. 5, is equivalent to study the Oldroyd-B constitutive relationships. Firstly, observe from Fig. 5a, as viscoelastic effects strengthen, the load increases linearly versus *De* for the Oldroyd-B model suggesting a weakly viscoelastic response (since the cone inclination angle is very small). However, the nonlinear Giesekus model predicts a saturation versus *De* as the secondary effects of finite extension and shear thinning dominate. Similarly, the net friction on the lower plate remains unaffected by the Oldroyd-B model but decreases versus *De* in the nonlinear case due to shear thinning.

More importantly is the effect of misalignment and asymmetry of the surface. Unlike the tilted cone in Fig. 3, where the maximum and minimum height of the cone changed significantly with the inclination angle δ, the factor *e* only slightly affects the surface height. Although we introduce a very weak effect by varying *e* from zero (fully aligned) to one, a significant change in the load is observed for both models while the friction remains unaffected. The load decreases versus *e* but remains positive for Oldroyd-B. Whereas, for Giesekus, depending on α, the load becomes negative. From an experimental point of view, a slight asymmetry in the surface, due to misalignment or other surface defects may result in an entirely incorrect assessment of the net force. The friction, and hence, the torque remains unaffected which may further mislead the results.

Afterwards we consider only the Oldroyd-B model and explore the range of high Deborah number. In Fig. 6, the pressure distribution over the misaligned tilted pad is given for $0 < De < 1.25$ using $\delta = 1.011°$, $e = 1$, $\beta = 0.8$. An observable asymmetry of the pressure is observed as De increases, favoring the cone tilt direction since the flow accelerates in that region (as the cross-sectional area reduces). This movement of the pressure peak reflects the subtle advection of the stretched polymers, and, therefore, the normal stress, which induces a strong asymmetry in the pressure distribution beyond what the small tilt induces. When the flow is Newtonian ($De = 0$), the load produced by a small misalignment ($e << 1$) is negligible. This implies that the surface is still appreciably flat. However, for a viscoelastic fluid, these small variations reflect strongly in the load carrying capacity. We remark here again that the friction was not affected.

In Fig. 7a, we show the net vertical force scaled with the Deborah number versus the tilt for different De. For small e (a well aligned channel without surface asymmetry), the results are perfectly linear. A disparity arises when we increase the degree of misalignment. If we increase the Deborah number further, depicted in Fig. 7b, we find a strong onset of a nonlinear trend in the load when $De > 2$. A saturation in the load occurs, similar to the sliding Cartesian configuration (Ahmed and Biancofiore 2021), followed by an eventual reduction.

Lastly, from a numerical perspective, despite the simplistic choice of the surface and an accurate *apriori* estimation of the Newtonian velocity field, the numerical solution of the constitutive relations still becomes unstable for very large values of the Deborah number. Nonetheless, the ultra-dilute assumption was effective in decoupling the system of equations and greatly increasing the computational efficiency. It is possible that global methods such as the pseudo-spectral method could prove more efficient. However, the onset of elastic instabilities cannot be ruled out, as the critical Deborah number may be comparable to the largest De explored in this study (Pakdel and McKinley 1996; McKinley et al. 1996; Castillo-Sánchez et al. 2022). Such instabilities could, in principle, hinder the convergence of the numerical algorithm to a steady solution. A detailed investigation of this aspect lies beyond the scope of the present work and will be addressed in future studies.

Textured pad

Textured surfaces reduce friction and increase load carrying capacity. The size and shape of the surface textures improve their positive effect. In this section, we present results for (i) symmetric and smooth and (ii) asymmetric sharp textures (Schuh et al. 2017) using only the Oldroyd-B constitutive equation. The latter pocket type exhibits a net increment to the load carrying capacity and reduction in friction even for Newtonian fluids, but is arguably numerically challenging. We explore the feasibility of using the VR model under the ultra-dilute assumption to study such surfaces given the inherent numerical complexity of resolving abruptly varying surface profiles. For the inclined pocket case, we have included also a comparison to the results of Schuh et al. (2017) for the Newtonian case.

Straight pockets

The cylindrical pocket are smoothed by using the function s

$$s = \frac{1}{2}\left(1 - \tanh\left(w_p \frac{\sqrt{(x-x_c)^2 + (y-y_c)^2} - r_p}{2}\right)\right) \tag{20}$$

where, $w_p = 0.05$ is the width of the smoothed edge, $r_p = 0.2$ is the radius of the pocket and (x_c, y_c) are the coordinates of the center of the pocket. The final shape is found by multiplying s with the cylindrical pocket

$$\begin{aligned} h = 1 \quad \text{if } \sqrt{(x-x_c)^2 + (y-y_c)^2} > r_p \\ \text{and} \quad h = 1 + d_p \text{ otherwise,} \end{aligned} \tag{21}$$

where $d_p = 0.2$ is the depth of the pocket. Figure 8(a) shows a cylindrical pad with ten equally spaced pockets with edges that are smoothed.

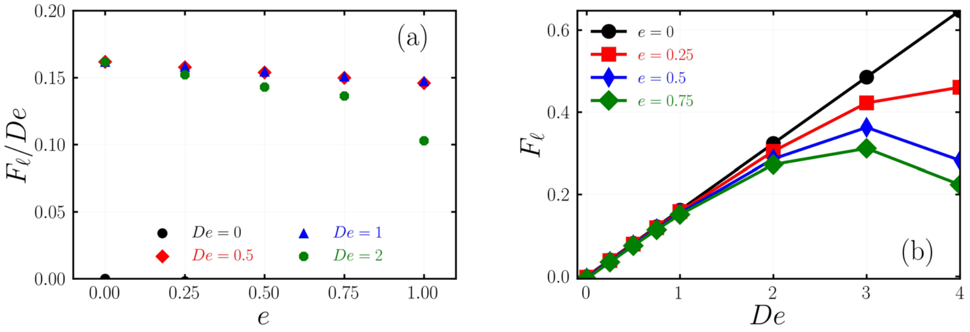

Fig. 7 The variation in the load carrying capacity scaled versus (a) the misalignment coefficient e and (b) the Deborah number for $\delta = 1.011°$, $\beta = 0.8$, and $\alpha = 0$

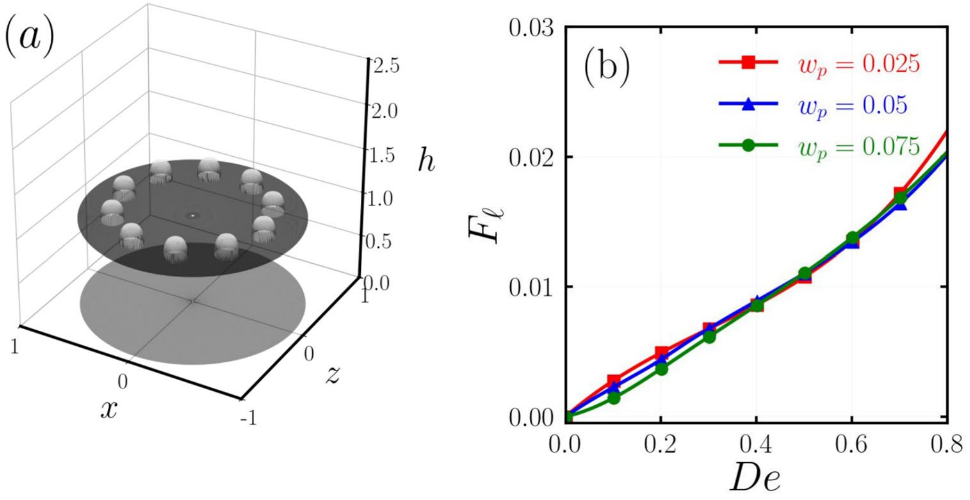

Fig. 8 A flat cylindrical pad lined with ten symmetric pockets with smoothed edges $w_p = 0.05$, $r_p = 0.1$, $d_p = 0.1$ and (b) the load carrying capacity versus the Deborah number, varying the width of the smoothed edges of the pockets

For this configuration, the load carrying capacity versus the intensifying viscoelasticity of the lubricant is predicted in Fig. 8(b) for different values of the edge width (decreasing w_p sharpens the pocket boundary). Firstly, we note that the net force increases considerably above the Newtonian baseline of zero. For a symmetric pocket, the Newtonian case unsurprisingly produces an antisymmetric pressure distribution, summing to zero upon integration over the area, but the advective nature of the viscoelastic stresses (Ahmed and Biancofiore 2021) leads to a net positive force that varies nonlinearly with *De*. Steepening the pocket edges (decreasing w_p) increases the load slightly indicating that the major contribution of the stresses is produced within the core of the pocket as opposed to its boundaries.

Numerically, pockets with smooth edges are less challenging and convergence is achieved over a wide range of *De* and geometric parameters. However, local effects that lead to physical and numerical instability that might arise close to sharp and straight edges are naturally eliminated. We observe that further steepening the edges of the pocket by setting $w_p = 0.0025$ gives $F_\ell = 0.0047$ for $De = 0.2$, an increase of 7% above the smoother case; $w_p = 0.025$ and $F_\ell = 0.0044$. For practical purposes, the use of smooth pockets can incur inaccuracy of a few percent points over the exact sharp case, but is sufficient to extract the trend in load versus the Deborah number. More importantly, we demonstrate that the onset of viscoelasticity in the lubricant increases the load carrying capacity well above the Newtonian baseline.

Inclined pockets

Asymmetric pockets with sharp straight edges give a finite load in the Newtonian case. We modify the cylindrical texture from Eq. 20

$$D = 2R_0 \sin\beta, \tag{22a}$$

$$Y = 2R_0 \cos\beta - R_0, \tag{22b}$$

$$\theta_\beta = t_0 + \arctan\left(\frac{Y}{r_0}\right), \tag{22c}$$

$$h(\theta) = \begin{cases} \dfrac{D}{\theta_\beta - \theta_{\min}}(\theta - \theta_{\min}), & \theta_{\min} \le \theta \le \theta_\beta, \\ \dfrac{D}{\theta_{\max} - \theta_\beta}(\theta_{\max} - \theta), & \theta_\beta \le \theta \le \theta_{\max}, \\ 0, & \text{otherwise}, \end{cases} \tag{22d}$$

where, θ_{min} and θ_{max} are the start and end of the pocket. Using Eqs. 22, the textures employed in Schuh et al. (2017) are obtained. However, owing to the numerical challenge in dealing with the sharp edges of the texture, we apply the same smoothing function *s* utilised for the straight pocket (see Eq. 20). We depict in Figs. 9(a)-(d) the textured pad analysed for varying texture angles. Furthermore, a validation of the numerical procedure which relies on the finite difference method is depicted in Figs. 9(b) which shows a comparison between this work and the results from literature of the load carrying capacity (or net vertical force) exerted on the pad versus the inclination angle of the textures (β_t) for a Newtonian fluid.

We find a good agreement between our results using the classical finite difference method and the pseudo-spectral method used in Schuh et al. (2017) over the entire range of the texture angle, β_t. Moreover, the variation in the normal force is smooth and free of any discrepancies for steeper textures. A small difference is observed between the results which is attributed to (i) the different numerical schemes adopted in this work and (ii) the use in our work of the full circular pad as opposed to a single periodic texture as in Schuh et al. (2017). In the latter case, only a single texture is simulated (using a highly resolved mesh).

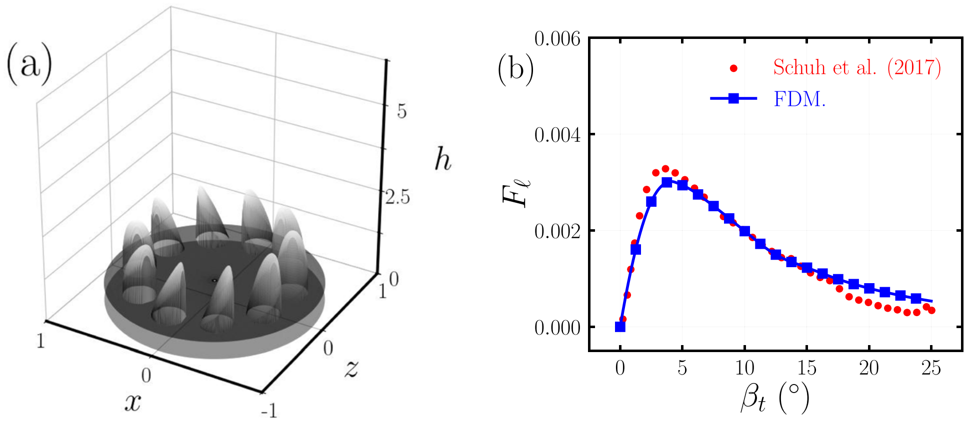

Fig. 9 (a) The cylindrical textured pad with smoothed asymmetrical textures inclined at $\beta_t = 7.5°$, and (b) the net vertical force exerted on the pad versus the inclination of the textures using the finite difference method compared with the results from Schuh et al. (2017) (Hoon Lee et al. 2017) for a Newtonian fluid. The textures in this study were smoothed using the function s, see Eq. 20

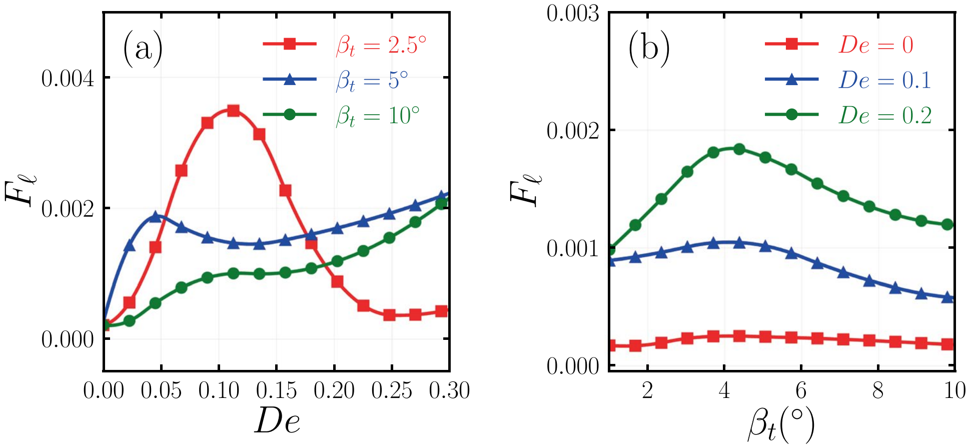

Fig. 10 The variation of the net vertical force exerted on the pad embedded with smooth inclined textures versus (a) the Deborah number for different angles of inclination and (b) the angle of inclination of the texture for different *De* using $\beta = 0.2$, $\alpha = 0$

We now introduce a viscoelastic lubricant for the same textured pad and examine the variation of the load with the Deborah number, shown in Fig. 10(a), and with the texture inclination angle, shown in Fig. 10(b), for $\epsilon = 0.01$ and $\beta = 0.8$. An initial increase in load is observed as polymer elasticity strengthens, and this increment remains significant across the entire range of *De* examined. This indicates that elastic polymers enhance load generation beyond the Newtonian case, where only viscous forces are present. The additional gain arises from finite normal stresses in the radial and circumferential directions. At larger *De*, however, the load response becomes strongly nonlinear and highly sensitive to β_t. A general trend emerges: (i) for low β_t, the load reaches a maximum before decreasing, while (ii) for higher β_t, the decrease is less steep and may eventually be followed by a secondary rise at large *De*. Moreover, viscoelasticity amplifies the effect of the texture inclination angle, as seen in Fig. 10b.

From a numerical perspective, the smooth edges allow the simulations to converge even for relatively large values of the Deborah number and steep texture angles. However, a difference in the load carrying capacity is expected as *De* grows, for example, a 7% difference was recorded for the symmetric pocket case in Section "Straight pockets" for $De = 0.2$ and $w_p = 0.025$. Generally, the VR approach fails to reach a steady state (or the iterative procedure stagnates/slows down) when the value of *De* reaches $De \sim 1$. We attribute this failure to a numerical instability typical of simulations of viscoelastic flows, however we cannot disregard the onset of elastic instabilities (Castillo-Sánchez et al. 2022) either for the textured pad at this value of the Deborah number. Linearized models in *De* are typically used for such studies (Li 2014) (assuming their validity when *De* is small), but we demonstrate the variation of the load can be strongly nonlinear depending on the angle of inclination of the texture. Finally, we remark that the classical finite difference method (or any mesh-based approach) will require large mesh sizes to capture the full pad which greatly increases the amount of computer memory required. However, global approaches such as the pseudo-spectral or collocation methods could offer more computationally efficient alternatives (Schuh et al. 2017).

Conclusions and future work

In this work, we have examined the influence of fluid viscoelasticity on the load carrying capacity and friction using the cylindrical viscoelastic Reynolds equation in the ultra-dilute limit using the linear Oldroyd-B and Giesekus constitutive relations. We considered two geometric configurations ideally suited for the cylindrical coordinate system: an inclined (mis)aligned cone mimicking a cone-and-plate rheometer and a textured pad.

The results for the inclined cone show a strong change in the load and friction versus the angle of inclination. However, pressure was produced (identically zero in the Newtonian case) only due to the circumferential normal stress component. In contrast, when we introduced a small degree of misalignment due to which the surface height varied along r and θ, the predicted load changed quite considerably while friction was less affected. In particular, for the nonlinear Giesekus constitutive model, negative values were observed in comparison to a positive load for a fully aligned cone.

We introduce first a textured pad with straight smoothened cylinder pockets. Interestingly, the load carrying capacity, that will be zero for the Newtonian case, increases with *De*. Conversely, the pad with the inclined pockets shows a strong non-linear behaviour and a general increase in the load due to viscoelasticity compared to the non-zero Newtonian case. The variation in the load versus the texture angle of inclination mimicked the pattern for the Newtonian distribution with a net increase depending on *De*.

Despite the significantly simplified form of the VR using an *apriori* estimate of the velocity field and a fully-implicit numerical algorithm, the problem still proved challenging as *De* increased. Convergence for larger values was not reached either for the cone and plate configuration or the textured pads. This failure is attributed to either an early onset of the HWNP or to the onset of an elastic instaiblity (Castillo-Sánchez et al. 2022).

In addition the use of the finite difference method which may not be the best option for the cylindrical coordinate system. The use of global methods such as the pseudo-spectral method may achieve more success. We believe, for smoother surfaces, the ultra-dilute approximation and the VR model is a good combination to study viscoelastic fluid flow through thin contacts conforming to cylindrical coordinates. Modeling the thin contact between bubbles, soft surfaces, joints etc. can be efficiently performed via this approach.

Appendix A: Deriving the viscoelastic Reynolds model

In this section, we present a brief derivation of the viscoelastic Reynolds (Eq. 9) in the cylindrical coordinate system. We follow the procedure for the Cartesian coordinate system from Ahmed and Biancofiore (2021) and extend it to three dimensions. Beginning with the scalar Eqs. 4a-4j, we integrate the r and θ momentum equations twice (subject to the no-slip boundary conditions 10a-10b) to get,

$$u_r = \frac{1}{2\beta}\frac{\partial p}{\partial r} + \frac{1}{\beta}\left(-\int_0^z\int_0^z \mathcal{R}\,dz^{'}dz + \frac{z}{h}\int_0^h\int_0^z \mathcal{R}\,dz^{'}dz\right), \tag{A1a}$$

$$u_\theta = \frac{1}{2\beta r}\frac{\partial p}{\partial \theta} + r\left(1-\frac{z}{h}\right) + \frac{1}{\beta} \left(-\int_0^z\int_0^z \mathcal{T}\,dz^{'}dz + \frac{z}{h}\int_0^h\int_0^z \mathcal{T}\,dz^{'}dz\right), \tag{A1b}$$

$$\mathcal{R} = \frac{1}{r}\frac{\partial}{\partial r}(r\tau_{rr}) + \frac{1}{r}\frac{\partial \tau_{\theta r}}{\partial \theta} + \frac{\partial \tau_{zr}}{\partial z} - \frac{\tau_{\theta\theta}}{r}, \tag{A1c}$$

$$\mathcal{T} = \frac{1}{r^2}\frac{\partial}{\partial r}(r^2\tau_{r\theta}) + \frac{1}{r}\frac{\partial \tau_{\theta\theta}}{\partial \theta} + \frac{\partial \tau_{z\theta}}{\partial z}. \tag{A1d}$$

Substituting Eqs. A1a-A1b into the continuity equation and integrating across in accordance with the Leibnitz theorem yields an integral differential equation for the pressure,

$$\frac{1}{r}\frac{\partial}{\partial r}\left(\frac{rh^3}{12}\frac{\partial p}{\partial r}\right) + \frac{1}{r}\frac{\partial}{\partial \theta}\left(\frac{h^3}{12r}\frac{\partial p}{\partial \theta}\right) = \frac{1}{r}\frac{\partial \mathcal{G}}{\partial \theta} + \frac{1}{r}\frac{\partial (r\mathcal{F})}{\partial r} \tag{A2a}$$

$$\mathcal{F} = \mathcal{C}\left(\frac{1}{r}\frac{\partial (r\tau_{rr})}{\partial r}\right) + \mathcal{C}\left(\frac{1}{r}\frac{\partial \tau_{\theta r}}{\partial \theta}\right) + \mathcal{C}\left(\frac{-\tau_{\theta\theta}}{r}\right) + \mathcal{D}(\tau_{zr}), \tag{A2b}$$

$$\mathcal{G} = \frac{\beta}{2}rh + \mathcal{C}\left(\frac{1}{r^2}\frac{\partial (r^2\tau_{r\theta})}{\partial r}\right) + \mathcal{C}\left(\frac{1}{r}\frac{\partial \tau_{\theta\theta}}{\partial \theta}\right) + \mathcal{D}(\tau_{z\theta}), \tag{A2c}$$

$$\mathcal{C}(\cdot) = \int_0^h \frac{z}{h}\int_0^h\int_0^{z^{'}} (\cdot)\,dz^{'}dzdz - \int_0^h\int_0^{z^{''}}\int_0^{z^{'}} (\cdot)\,dz^{'}dz^{''}dz, \tag{A2d}$$

$$\mathcal{D}(\cdot) = \int_0^h \frac{z}{h}\int_0^h (\cdot)\,dz^{'}dz - \int_0^h\int_0^{z^{'}} (\cdot)\,dz^{'}dz. \tag{A2e}$$

Note that

$$\int_0^h \frac{\partial u_z}{\partial z}dz = u_z(r,\theta,h) - u_z(r,\theta,0) = 0. \tag{A3}$$

The integral operators, $\mathcal{C}$ and $\mathcal{D}$, are identical to those in the Cartesian coordinate configuration and are a general representation of the model (Ahmed and Biancofiore 2023). However, we can further simplify Eq. by (i) applying integration by parts (Hinch et al. 2024) and (ii) switching to the computational configuration; $h(r,\theta) = H(R,\Theta)$, $z = ZH(R,\Theta)$,

$$\int_0^h \int_0^{z'} q\, dz'\, dz = h^2 \int_0^1 (Z-1) q dZ = h^2 \overline{[(Z-1)q]}, \tag{A4a}$$

$$\int_0^h \frac{z}{h} \int_0^h q\, dz'\, dz = \frac{h^2}{2} \overline{[q]}, \tag{A4b}$$

$$\int_0^h \int_0^{z'} \int_0^{z''} q\, dz''\, dz'\, dz = h^3 \int_0^1 \int_0^{Z'} \int_0^{Z''} q\, dZ''\, dZ'\, dZ \tag{A4c}$$

$$= h^3 \overline{\left[(\frac{Z}{2} - Z + \frac{1}{2}) q \right]},$$

$$\int_0^h \frac{z}{h} \int_0^{z'} \int_0^{z''} q\, dz''\, dz'\, dz = h^3 \overline{\left[(-\frac{Z}{2} + \frac{1}{2}) q \right]}, \tag{A4d}$$

for the quantity q, yielding (upon substitution into Eqs. A2a and A2c)

$$\frac{1}{r}\frac{\partial}{\partial r}\left(\frac{r h^3}{12} \frac{\partial p}{\partial r} \right) + \frac{1}{r} \frac{\partial}{\partial \theta} (\frac{h^3}{12} \frac{\partial p}{\partial \theta}) = \frac{1}{r} \frac{\partial \mathcal{G}}{\partial \theta} + \frac{1}{r} \frac{\partial (r \mathcal{F})}{\partial r}, \tag{A5a}$$

$$\mathcal{F} = \frac{h^3}{2} \overline{\left[(Z - Z^2) \frac{1}{r} \frac{\partial (r \tau_{rr})}{\partial r} \right]} + \frac{h^2}{2} \overline{[(2Z-1)\tau_{rz}]} \tag{A5b}$$

$$+ \frac{h^3}{2} \overline{\left[(Z - Z^2) \frac{1}{r} \frac{\partial \tau_{r\theta}}{\partial \theta} \right]} - \frac{h^3}{2} \overline{\left[(Z - Z^2) \frac{\tau_{\theta\theta}}{r} \right]},$$

$$\mathcal{G} = \frac{\beta}{2} r H + \frac{h^3}{2} \overline{\left[(Z - Z^2) \frac{1}{r^2} \frac{\partial (r^2 \tau_{r\theta})}{\partial r} \right]} \tag{A5c}$$

$$+ \frac{h^2}{2} \overline{[(2Z-1)\tau_{z\theta}]} + \frac{h^3}{2} \overline{\left[(Z - Z^2) \frac{1}{r} \frac{\partial \tau_{\theta\theta}}{\partial \theta} \right]}.$$

Acknowledgements The authors would like to acknowledge the Turkish National Research Agency (TÜBİTAK) for supporting this work under the project 221N576.

Funding Open access funding provided by Università degli Studi dell'Aquila within the CRUI-CARE Agreement.

Declaration

Conflicts of interest The authors report financial support was provided by Scientific and Technological Research Council of Turkey.

References

Ahmed H, Biancofiore L (2021) A new approach for modeling viscoelastic thin film lubrication. J Non-Newton Fluid Mech 292:104524

Ahmed H, Biancofiore L (2023) Modeling polymeric lubricants with non-linear stress constitutive relations. J Non-Newton Fluid Mech 321:105123

Ahmed H, Biancofiore L (2025) Viscoelastic thin-film lubrication in finite-width channels. J Fluid Mech 1018:16

Ahmed H, Biancofiore L (2022) A modified viscosity approach for shear thinning lubricants. Phys Fluids 34(10)

Akyildiz FT, Bellout H (2004) Viscoelastic lubrication with Phan-Thein-Tanner fluid (PTT). J Trib 126(2):288–291

Bird RB, Armstrong RC, Hassager O (1987) Dynamics of polymeric liquids. Fluid mechanics, vol 1

Boyko E, Stone HA (2021) Reciprocal theorem for calculating the flow rate-pressure drop relation for complex fluids in narrow geometries. Phys Rev Fluids 6(8):081301

Boyko E, Stone HA (2022) Pressure-driven flow of the viscoelastic Oldroyd-B fluid in narrow non-uniform geometries: analytical results and comparison with simulations. J Fluid Mech 936:23

Boyko E, Hinch J, Stone HA (2024) Flow of an Oldroyd-B fluid in a slowly varying contraction: theoretical results for arbitrary values of Deborah number in the ultra-dilute limit. J Fluid Mech 988:10

Castillo-Sánchez HA, Jovanović MR, Kumar S, Morozov A, Shankar V, Subramanian G, Wilson HJ (2022) Understanding viscoelastic flow instabilities: Oldroyd-B and beyond. J Non-Newton Fluid Mech 302:104742

Dowson D, Taylor C (1979) Cavitation in bearings. Annu Rev Fluid Mech 11(1):35–65

Fattal R, Kupferman R (2004) Constitutive laws for the matrix-logarithm of the conformation tensor. J Non-Newton Fluid Mech 123(2–3):281–285

Hinch J, Boyko E, Stone HA (2024) Fast flow of an Oldroyd-B model fluid through a narrow slowly varying contraction. J Fluid Mech 988:11

Hirsch C (2007) Numerical computation of internal and external flows: the fundamentals of computational fluid dynamics. Elsevier.

Hoon Lee Y, Schuh JK, Ewoldt RH, Allison JT (2017) Enhancing full-film lubrication performance via arbitrary surface texture design. J Mech Des 139(5):053401

Housiadas KD, Beris AN (2023) Lubrication approximation of pressure-driven viscoelastic flow in a hyperbolic channel. Phys Fluids 35(12)

Housiadas KD, Beris AN (2024) Viscoelastic flow with slip in a hyperbolic channel. J Rheol 68(3):415–428

Johnson KL, Tevaarwerk JL (1977) Shear behaviour of elastohydrodynamic oil films. Proc R Soc London A Math Phys Sci 356(1685):215–236

Lee YH, Schuh JK, Ewoldt RH, Allison JT (2019) Simultaneous design of non-Newtonian lubricant and surface texture using surrogate-based multiobjective optimization. Struct Multidiscip Optim 60:99–116

Li X (2014) Non-Newtonian lubrication with the Phan-Thien-Tanner model. J Eng Math 87:1–17

Lombardi L, Calabrese P, Tammaro D, Maffettone PL (2025a) Morphological dynamics of thin liquid films formed by bubbles oscillating near a free surface: experimental and numerical investigation. J Colloid Interface Sci 683:139–149

Lombardi L, Tammaro D, Maffettone PL (2025b) Wimpled thin films via multiple motions of a bubble decorated with surface-active molecules. J Colloid Interface Sci 677:521–528

McKinley GH, Pakdel P, Öztekin A (1996) Rheological and geometric scaling of purely elastic flow instabilities. J Non-Newton Fluid Mech 67:19–47

Moore MN, Shelley MJ (2012) A weak-coupling expansion for viscoelastic fluids applied to dynamic settling of a body. J Non-Newton Fluid Mech 183:25–36

Mortier RM, Orszulik ST, Fox MF (2010) Chemistry and technology of lubricants, vol 107115. Springer

Owens RG, Phillips TN (2002) Computational rheology. World Scientific

Pakdel P, McKinley GH (1996) Elastic instability and curved streamlines. Phys Rev Lett 77(12):2459

Phan-Thien N, Tanner RI (1983) Viscoelastic squeeze-film flows–Maxwell fluids. J Fluid Mech 129:265–281

Sari MH, Putignano C, Carbone G, Biancofiore L (2024) The effect of fluid viscoelasticity in soft lubrication. Tribol Int 195:109578

Sawyer WG, Tichy JA (1998) Non-Newtonian lubrication with the second-order fluid. J Tribol 120(3):622–628

Schuh JK, Ewoldt RH (2016) Asymmetric surface textures decrease friction with Newtonian fluids in full film lubricated sliding contact. Tribol Int 97:490–498

Schuh JK, Ewoldt RH (2019) Low Reynolds number friction reduction with polymers and textures. J Nonnewton Fluid Mech 273:104167

Schuh JK, Lee YH, Allison JT, Ewoldt RH (2017) Design-driven modeling of surface-textured full-film lubricated sliding: validation and rationale of nonstandard thrust observations. Tribol Lett 65:1–17

Szeri AZ (2010) Fluid film lubrication. Cambridge University Press

Tanner RI (1969) Increase of bearing loads due to large normal stress differences in viscoelastic lubricants. J Appl Mech 36(3):634–635

Tichy JA (1996) Non-Newtonian lubrication with the convected maxwell model. J Tribol 118(2):344–348

Tichy JA, Bou-Saïd B (2008) The Phan-Thien and Tanner model applied to thin film spherical coordinates: applications for lubrication of hip joint replacement. J Biomech Eng 130(2):021012

Venkatesh A, Anand V, Narsimhan V (2022) Peeling of linearly elastic sheets using complex fluids at low Reynolds numbers. J Non-Newton Fluid Mech 309:104916

Zhang H, Zhang W, Wang X, Li Y, Li X, Li F (2023) On the role of tensor interpolation in solving high-Wi viscoelastic fluid flow. Phys Fluids 35(3)

Zheng Z, Xie H, Chen X, Liu X, Yang W, Xu Y, Huang W (2023) Squeeze flow of a Maxwell fluid between two parallel disks or two spheres. Phys Fluids 35(8)